Supplementary Methods

Surgery. Mice were anaesthetized with ketamine/xylazine (100mg/kg / 10mg/kg, Sigma-Aldrich), and temperature was maintained at 37 degrees C on a feedback-controlled heating pad (Fine Science Tools). The scalp was removed, and membrane overlying the skull was cleared using a microblade (Roboz). An aluminum headpost cut from square bar (Small Parts, Inc.) was attached to the skull using RelyX luting cement (Henry Schein). The borders of the exposure were covered with silicone sealant (VWR). For dorsal glomeruli, the skull overlying the olfactory bulb was thinned using a dental drill (KaVo) and removed with forceps, and the dura was peeled back using fine forceps (Roboz). For lateral glomeruli, the skin overlying the cheek and zygomatic bone was removed, and vessels were cauterized (Fine Science Tools). The muscle attached to the zygomatic was peeled away, and the bone was removed with microscissors (Roboz). The eye and surrounding tissue was removed with microscissors; bleeding was stopped using gelfoam (Henry Schein), and animals were administered 0.7cc Ringer's solution (Henry Schein). The skull overlying the bulb was thinned and removed, and the dura peeled away. After electroporation, the bulb was coverslipped and covered in 2% agarose (Sigma-Aldrich), the exposure was covered in lidocaine jelly (Henry Schein) and then silicone sealant. Buprenorphine (0.05 mg/kg, Henry Schein) was administered after the animal could right itself. Animals recovered for 5 days after electroporation, and were then deeply anaesthetized with ketamine/xylazine and sacrificed by paraformaldehyde perfusion.

Electroporation. Animals were placed under a two-photon microscope (Ultima, Prairie Technologies), and a 16x objective was used to focus on a single glomerulus (.8NA, Nikon). A Ti-Sapphire laser (Coherent) was tuned to 880nm for experiments. Pulled glass pipets (Sutter, 5-6 μM tip) were backfilled with either lysine-fixable tetramethylrhodamine (TMR) dextran (3000 MW, 12.5 mg/ml in PBS) with biotin or lysine-fixable fluorescein (FITC) dextran (3000 MW, 12.5 mg/ml in PBS) with biotin (Invitrogen), and filled halfway with 0.9% w/v NaCl. The pipet was mounted on an electrode holder (WPI)/manipulator (Luigs and Neumann), and its tip was directed to the three-dimensional center of a glomerulus under two-photon guidance. Current was applied to the pipet using a stimulator (50V, 30msec pulses, at 2HZ, repeated 2-4 times, Grass SD-9 stimulator). The black lead of the stimulator was connected to the animal via an alligator clip on the foot. Note that while we observed robust and reliable long-range diffusion/transport of TMR dextran from labeled mitral and tufted cells to the olfactory cortex under these electroporation conditions, FITC dextran exhibited substantively less diffusion/transport (e.g. few or no labeled fibers in the LOT), which precluded the use of FITC dextran to explore axonal projections from the bulb to the cortex. Animals in which the glomeruli was not clearly labeled, the labeling was non-specific (an exceedingly rare occurance) or in which labeled mitral cells in the mitral cell layer could not be identified during the course of the experiment were excluded from subsequent analysis.

Histological processing. Animals were sacrificed by transcardial perfusion with 13ml PBS, followed by 10ml 1% paraformaldehyde. Brains were extracted and processed differentially depending on the region to be imaged. For imaging of the whole olfactory

cortex, the left hemisphere was discarded, and the subcortical matter of the right hemisphere was removed using forceps. Cortical tissue above the rhinal sulcus was dissected away, and guide cuts were made with a needle blade (Fine Science Tools). The ventral hemisphere (which includes all of the structures in the olfactory cortex) was then flattened between two slides separated by a 600 micron spacer constructed of #1.5 coverslips. The sample was placed in 4% paraformaldehyde overnight, and then stored in PBS until antibody staining. For imaging of the amygdala, the brain was dissected as previously described, and a needle blade was used to cut along the lateral olfactory tract to excise the olfactory tubercle; an additional cut was made above the cortical nuclei of the amygdala to excise the olfactory amygdala. We use this en bloc preparation of the amygdala to avoid distortions that occur at the ventral edge of the flattened hemi-preparation, where the cortical amygdala resides. This distortion is minimal in the center of the flattened preparation where the piriform cortex is located. The amygdala was fixed in 4% paraformaldehyde overnight, and then stored in PBS until antibody staining. Before application of antibody, samples were soaked in glycine (1.87grams/500ml PBS, Sigma-Aldrich) for 2 hours, followed by 1 hour in PBS, 30 minutes in sodium borohydride (0.4g/400ml PBS, Sigma-Aldrich) and 1 hour in PBS to quench autofluorescence. The following series of antibodies and washes were then used: primary antibody for 3 days (1:500 rabbit anti-tetramethylrhodamine, Invitrogen) in block (2% Triton X-100, 1% bovine serum albumin in PBS), wash 1 day (2% Triton X-100/PBS), secondary antibody for 2 days (1:250 goat anti-rabbit in block, Jackson Immunoresearch), wash 1 day, and tertiary antibody (1:250 TMR-conjugated donkey anti-goat in block, Jackson Immunoresearch) and counterstain (1:150 NeuroTrace 435 in

block, Invitrogen) for 2 days, followed by 1 day of wash. Samples were mounted in Vectashield (Vector Labs) on a slide with the shallow end of a Lab-Tek chambered coverglass as a coverslip (NUNC).

Quantification of Cellular Labeling. Two different methods were used to quantify the efficiency of our labeling method. First, after electroporation, we acquired z-stacks from the surface of the olfactory bulb through the mitral cell layer of the bulb (see Supplementary Movie 1), and used these z-stacks to count the number of cell bodies labeled in the mitral cell layer of the olfactory bulb post hoc. We were unable to quantify the number of tufted cells labeled for technical reasons: the brightness and number of cells labeled superior to the mitral cell layer, as well as the brightness of the glomerulus, made it difficult to quantify cell bodies (Suppl. Fig. 1), and the diversity in morphology and location of tufted cells made it difficult to identify them based on visual and depth criteria. Second, previous work has suggested that mitral cell axons travel superior to tufted cell axons in a segregated manner in the LOT and, unlike tufted cell axons, project to areas posterior to the anterior piriform cortex and olfactory tubercle (see Haberly et al, Brain Res 129:152, Scott et al, J. Comp Neuro 194:519, Scott J. Neurophys 46:918, Schneider et al, J. Neurophys 50:358, Skeen et al, J. Comp Neuro 172:1). We observed that near the most posterior aspect of the olfactory tubercle, the axons of presumed mitral cells form a distinct bundle that continues to travel past the tubercle towards the posterior piriform cortex and amygdala (Suppl. Fig. 2a). Therefore, we counted axons corresponding to presumed mitral cells in the posterior aspect of the LOT using a confocal microscope (see Suppl. Fig. 2). We did not quantify the number of presumed

tufted cells with this method due to technical constraints: these individual axons were difficult to optically resolve due to the large number of cells labeled, the high intensity of labeling, their smaller diameter, and the more three-dimensional structure of the presumed tufted cell axon band in the LOT.

Image acquisition. Images were acquired on a Zeiss 710 confocal microscope (Zeiss) using a 10x water immersion objective (Zeiss 0.45NA) or a Prairie In Vivo microscope using an 10x water immersion objective (Olympus 0.6NA). In both cases images were acquired in multiphoton mode using a Coherent laser tuned to 810 nm. Zen software with a custom-written macro was used for acquisition and tiling of images online; LSM 510 software was used for tiling in the event that it needed to be performed post-hoc (Zeiss). Images were also tiled using XUVTools (Albert-Ludwigs-Universitat Freiburg, see Emmenlaur et al, J. Micro. 233:42, 2009). Images in which clearly labeled mitral cell fibers were not apparent in the lateral olfactory tract adjacent to the posterior piriform cortex were excluded from further study; in all such cases samples exhibited other signs of poor labeling (i.e. poorly filled axonal arbors).

Image alignment. During all image processing the operator was blind to the glomerular identity of the particular image stack. Z-stacks of images of en bloc preparations of the cortical amygdala were aligned using an intensity-based, two-step, linear-nonlinear protocol. Image alignment was carried out in Statistical Parametric Mapping 8 (SPM8) (available at www.fil.ion.ucl.ac.uk/spm), an open-source software package widely used in fMRI research. SPM is validated for a variety of registration tasks, including analysis

of the axonal projection patterns of olfactory projection neurons in Drosophila (see Datta et al., Nature 452: 473, 2008). The linear registration algorithm used a standard 12-parameter algorithm with Gauss-Newton optimization. The nonlinear registration modeled the spatial transformation with a set of basis functions, the discrete sine transformation (DST) and the discrete cosine transformation (DCT), of various spatial frequencies. Typically only a small number of nonlinear iterations were carried out (often less than 100) and the nonlinear regularization value was held relatively high (typically at 100, never below 1) which maximized the relative contribution of the linear alignment to the template. We generated a standardized template brain stack of the cortical amygdala by morphing 4 individual stacks onto a single high-quality image stack and then averaging the intensity of the resultant 5 individual stacks. This standardized reference stack was then used to warp all cortical amygdala stacks used in this study. Warping parameters were optimized for each image stack and the quality of warping was assessed by the overlap between the warped brain and the template image in the counterstained image channel only. The major landmarks in this preparation are the posterolateral cortical amygdala, the posteromedical cortical amygdala and the ventral edge of the posterior piriform cortex, all of which were used to judge alignment quality. Images that failed to align based on the counterstain were excluded from the dataset. After warp parameters were defined based upon the counterstained channel, the channel containing the TMR-dextran staining was warped using identical parameters. Because after warping most of the data was contained in superficial planes, all analysis was performed on a maximum intensity projection of the warped volume. Alignment of maximal intensity projections of image stacks of the piriform cortex (which were highly

anisotropic—i.e. 20,000 x 10,000 x 40—precluding accurate volumetric alignment by SPM8) was performed in Photoshop using affine commands (such as zoom and rotate) as well as the "Warp" command, using only the counterstain as a guide to position.

Statistics. All errorbars are +/- standard error of the mean (SEM). One-way MANOVA was used to test whether multivariate means of variables for different glomerulus types are different at the 0.05 significance level.

Image processing and cluster analysis. During all image processing the operator was blind to the glomerular identity of the particular image stack. Images were processed by using a semi-supervised algorithm to filament trace the raw warped image stacks using the Imaris software package (Bitplane), slightly dilating the filaments, and then using those slightly dilated filaments to mask the original raw data. Before extraction of parameters, piriform and posterolateral nucleus projection patterns were aligned using the image alignment procedure previously described. Samples that were unable to be aligned due to poor counterstain or extreme physical distortion were excluded from K-means analysis. The data were then maximally contrasted so that differences in label intensity were normalized. A number of parameters characterizing the features of the axonal projection patterns to the piriform cortex (x and y center of mass coordinates, x and y centroid coordinates, x-coordinate of most anterior fiber, y-coordinate of most posterior fiber at LOT, number of TMR-positive pixels) and amygdala (x and y center of mass coordinates, x and y centroid coordinates, x-coordinate of medial-most fiber, absolute fiber density within the lateral and medial hemispheres of PLCo, ratio of lateral/medial

fiber density to total fiber density within the PLCo) were extracted from the aligned and processed images of samples using ImageJ (NIH) and Matlab (The Mathworks). No combination of parameters led to correct classification by glomerular type for piriform images, but the following parameters could be used in various combinations with nearly equal measures of success to classify amygdala samples: X-coordinate of center of mass, X-coordinate of medial-most fiber, absolute fiber density within the medial hemisphere of PLCo, and the ratios of fiber density within the medial or lateral hemispheres to the total fiber density within the PLCo. The standardized Euclidean distance between pairs of objects in an M-by-N data matrix X, where rows of X correspond to the values of variables extracted from a single amygdala image and columns correspond to different variables, was then calculated using the "pdist" function in Matlab. The "linkage" function was then used to create a hierarchical cluster tree using the furthest distance between the clusters from the standardized Euclidean distance matrix calculated using "pdist". K-means clustering was performed using the "kmeans" function in Matlab, which partitions the points in the data matrix X into N clusters (e.g. N=3 for 3 glomeruli) by minimizing the sum, over all clusters, of the within-cluster sums of point-to-cluster centroid distances (squared Euclidean distance). The accuracy of this clustering is assessed by counting how many samples are correctly grouped together by glomerulus type. Calculation of the density of fibers was performed by generating a Z projection of the warped and processed images, and using the contour surface function of Imaris (Bitplane) to calculate the pixel density within the lateral and medial halves of the posterolateral cortical amygdala. The boundary between the lateral and medial halves of the poesterolateral nucleus was defined by the line extending straight horizontally

through the semimajor axis of the posteromedial nucleus (which appears as an ellipse in the warped template brain; see Fig. 4d).

Normalized cross-correlation. Images of piriform cortex and posterolateral cortical amygdala projection patterns were blurred using a Gaussian filter (PIR σ = 200 μM; AMG σ = ~70 μM), cropped to exclude areas outside the region of interest (e.g. Figs. 3a-3c, Fig.. 4d, white square), resized (PIR = 500 x 250 pixels; AMG = 200 x 224 pixels), thresholded in Photoshop (Adobe) to binarize pixel values, and converted to grayscale in Matlab. The "normxcorr2" function in Matlab was then used to compute the normalized cross-correlation between the pixel values of two images (e.g. MOR 1-3 piriform 1 x MOR 1-3 piriform 2) (Suppl. Fig. 8a). This function returns a matrix of Pearson correlation coefficients calculated using the following equation:

$$\gamma(u,v) = \frac{\sum_{x,y}\left[f(x,y) - \bar{f}_{u,v}\right]\left[t(x-u,y-v) - \bar{t}\right]}{\left\{\sum_{x,y}\left[f(x,y) - \bar{f}_{u,v}\right]^2 \sum_{x,y}\left[t(x-u,y-v) - \bar{t}\right]^2\right\}^{0.5}}$$

Where:

- f is the image.
- $\bar{t}$ is the mean of the template
- $\bar{f}_{u,v}$ is the mean of $f(x,y)$ in the region under the template.

By default, non-overlapping pixels in this analysis are assigned a padding value of zero; note that because the means of the template and the source image are subtracted from the pixel values, non-overlapping pixels can still potentially contribute to the correlation

coefficient. This matrix of correlation coefficients is then plotted using the "surf" function in Matlab to generate correlograms (Suppl. Fig. 8c), where warmer colors represent high correlation values (close to 1) and cooler colors represent anticorrelation values (close to -1). The cross-correlation between pixel values in two images was calculated when the images were directly superimposed, and calculated again as one image was shifted relative to the other until no more overlap is possible in all directions (Suppl. Fig. 8b). The result of these calculations is a matrix of correlation coefficients that reflects the degree of correlation between the pixel values in two images across the entire range of shifts (until the images are completely non-overlapping), and this matrix can be plotted as a correlogram (Suppl. Fig. 8c). If there is similarity in the spatial patterning in two images, there will be a peak (red color) in the correlogram that reflects correlation coefficients greater than zero. The location of this peak in the correlogram is a direct reflection of the similarity between the spatial patterning in two images. Images with similar spatial patterning will have the highest correlation in pixel values when they are directly superimposed, and the result of this is a peak at the center of the correlogram—the images do not need to be significantly shifted relative to each other for the spatial patterning to overlap. Images with dissimilar spatial patterning will have the highest degree of correlation in pixel values when one is shifted relative to the other (i.e. shifting one image relative to the other gets the patterning in the images to overlap), resulting in a peak in the correlogram that is displaced from the center. The amount the correlogram peak is spatially offset from the center of the correlogram can be quantified, and used as a measure of the similarity of the spatial patterning in two images (Suppl. Fig. 10, 11). Finally, the shape of the peak in the correlogram is related to the nature of

the patterning; focal patterning will generate a more focal (circular) peak, while more distributed patterning will generate a more elongated peak (i.e. there is overlap in the two patterns over a larger range of spatial shifts). For both piriform and amygdala, normalized cross-correlation was performed for all pairwise combinations, in both possible configurations (e.g. MOR 1-3 A x MOR 28 A, and MOR 28 A x MOR 1-3 A). The location of the maximum correlation coefficient in correlograms was determined by transforming the matrix of correlation values into a linear array and using the "max" function to find the maximum value in the array, followed by the data cursor feature to find the X and Y coordinates of the maximum correlation coefficient in each correlogram. For each pairwise comparison, the location of the maximum correlation coefficient for the configuration where the distance between the location of the maximum correlation coefficient and the center of the correlogram was the smallest was used to generate scatterplots.

Because non-overlapping pixels can potentially be assigned a real number value (due to subtracting of the means) in the calculation of the Pearson correlation coefficient, artifacts can be introduced in the correlogram at the edges, which represent correlation coefficients calculated under conditions where few pixels are overlapping between the template and the source images. We therefore also performed normalized cross-correlation analysis using an alternative data padding method to control for the possibility that the edge artifacts cause changes in the spatial position of the correlogram coefficient maximum. Template images tiled as a 3x3 array (Supplementary Figure 8d) were generated for all individual images, and the normalized cross-correlation was then calculated for all pairwise combinations of single and tiled images, as previously

described. Running the NormXCorr2 algorithm using the tiled templates returns a correlogram that resembles a 3x3 grid with additional data points at the edges, but in which the block in the center has been subject to analysis without the source image ever sliding off into a region that has no overlap. Because the template image is tiled, the region of overlap between the sliding image and the template will always contain the same set of pixel values, though the spatial order of these pixels will be offset. The result is that, for computing the center block of the 3x3 cross-correlogram, the mean image pixel value and the standard deviation of image pixel values used to calculate the Pearson coefficient are constant as this region of the tiled image slides across the template; this effectively avoids the introduction of the edge artifacts described above. The resulting matrices of correlation coefficients were plotted using the "surf" function. These matrices were either left uncropped (and therefore include the correlations between all 9 panels plus the edges), were cropped to the equivalent spatial displacements as were generated in the initial analysis with zero padding (and which therefore contain offset peaks that are directly comparable between the two methods), or were cropped such that the source image only was allowed to slide for 50% of its length on any axis across the template image. This final crop limits all of the values in the correlation matrix to those in which half or more of the values in the correlation matrix arise from correlations between the image and the center tile (rather than the adjacent tiles in the template). The X,Y coordinates of the maximum correlation coefficient were extracted from the "equivalent" correlograms using the "max" and "find" functions on a submatrix representing the correlation coefficient values within and surrounding the center peak of the correlogram (e.g. the peak closest to the center of the correlogram, not the peaks near the edge of the

correlogram in the equivalent view). Once again, for each pairwise comparison, the location of the maximum correlation coefficient for the configuration where the distance between the location of the maximum correlation coefficient and the center of the correlogram was the smallest was used to generate scatterplots. The scatterplots generated using the two different methods are qualitatively and quantitatively similar (Supplementary Figures 10,11; Supplementary Table 2,3), and the correlograms generated by the two methods are qualitatively similar as well (Supplementary Figure 12), suggesting that our analyses are robust to possible correlation artifacts caused by differences in the degree of pixel overlap between the two methods.

Genetics. Construction of MOR1-3-IRES-GFP animals was achieved as follows: A 7.8 kb genomic clone containing the complete MOR1-3 open reading frame plus 5.3 kb upstream and 1.5 kb downstream sequence was mutagenized by PCR to insert a PacI restriction site 5 bp after the stop codon. An IRES-GFP-ACN cassette was cloned into the PacI site to prepare the targeting vector (the ACN cassette is described in Bunting et al, Genes Dev 13: 1524, 1999.). Following electroporation into 129SvEv-derived mouse ES cells, genomic DNA from G418-resistant colonies was screened by Southern blotting with AflII to detect homologous recombination using a 400 bp probe 5' of the targeting vector (7.4 kb wild-type allele versus 12.7 kb targeted allele). Chimeras obtained from recombinant clones by standard mouse procedures were mated to C57BL/6J females to obtain heterozygous MOR1-3-IRES-GFP mice that had deleted the neo^R selection marker in the male germline. Construction of the MOR 174-9-IRES-GFP animals was achieved as follows: Two genomic fragments containing the MOR174-9 5' flanking sequence plus

open reading frame (3.4 kb, XmaI sites) and 3' flanking sequence (2.7 kb, SalI sites) were isolated by PCR from mouse genomic DNA, with restriction sites present in the primers. These two homologous arms were cloned into an IRES-GFP-ACN vector to obtain the targeting construct. Homologous recombinant clones were identified by EcoRI-digested genomic DNA blots (5.2 kb wild-type allele versus ~10 kb targeted allele) using a 300 bp probe 5' of the construct. Mice were obtained from recombinant ES cells as described for MOR1-3-IRES-GFP strain. MOR28-IRES-GFP was previously described (see Shykind et al, Cell 117:801, 2004). Note that MOR28 is also known as MOR 244-1. The OMP-IRES-spH and M72-IRES-GFP animals were obtained from the Jackson Labs.

Supplementary Information

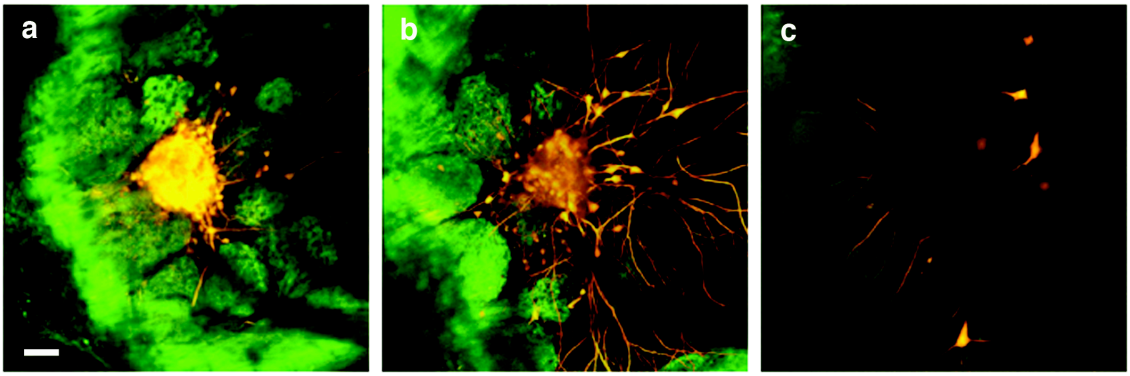

Supplementary Figure 1. Examples of TMR labeling at different depths in the olfactory bulb. (a) Z-projection of images taken in the glomerular layer of a bulb in which a single glomerulus has been electroporated with TMR dextran (red). A number of labeled periglomerular cells can be seen flanking the labeled glomerulus; note that often these cell bodies cannot be disambiguated from the glomerular border (scale bar = 60μM; green = synapto-pHluorin). **(b)** Z-projection of images taken in the external plexiform layer of the bulb. Several putative tufted cells can be seen to the right of the glomerulus. Note that the number of cells labeled, the distributed location and varying size of the cell bodies of the putative tufted cells, and the bright shadow of the labeled glomerulus make it difficult to accurately count the number of tufted cells labeled using our method. **(c)** Z-projection of images taken in the mitral cell layer of the bulb. The large cell body size,

the distinct laminar location of cell bodies, and their distance from the glomerular layer (~200 μM) make it possible to quantify the number of labeled cells in the mitral cell layer.

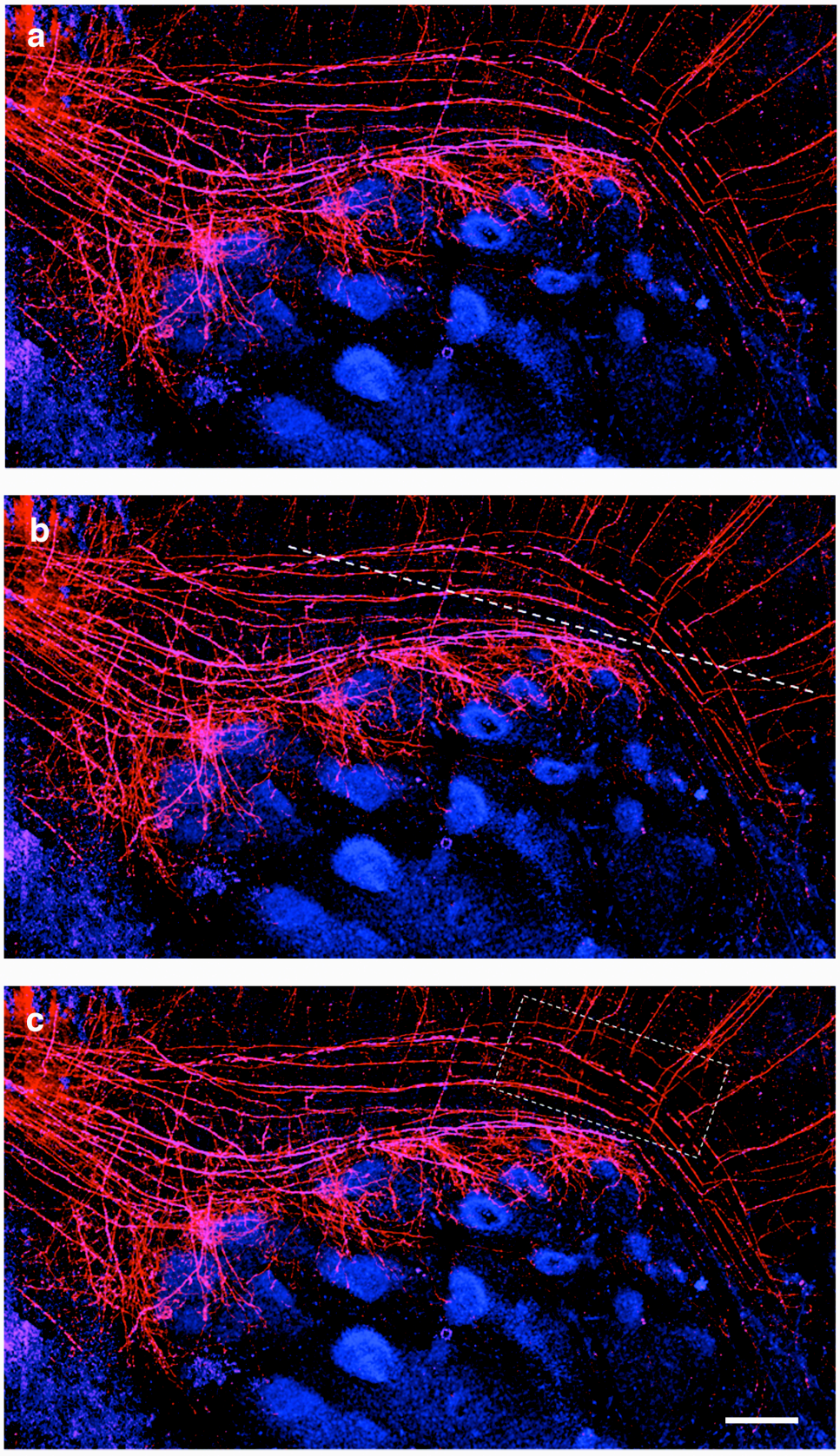
a
b
c

Supplementary Figure 2. Putative mitral cell and tufted cell axon streams are visually distinguishable in the posterior lateral olfactory tract. (a) The appearance of the LOT after the labeling of a single glomerulus with TMR dextran (scale bar = 400 μM). **(b)** Two separate axon fiber tracts can be distinguished in the posterior aspect of the LOT (separation highlighted by dotted line). **(c)** The fibers in the superior, putative mitral cell axon tract (yellow box) are quantified to control for differences in number of axons labeled using our method. The axons in this tract can be followed all the way to the cortical nuclei of the amygdala. The number of labeled axons we count in this tract are similar to the number of neurons in the mitral cell layer counted in z-stacks taken of the olfactory bulb after electroporation.

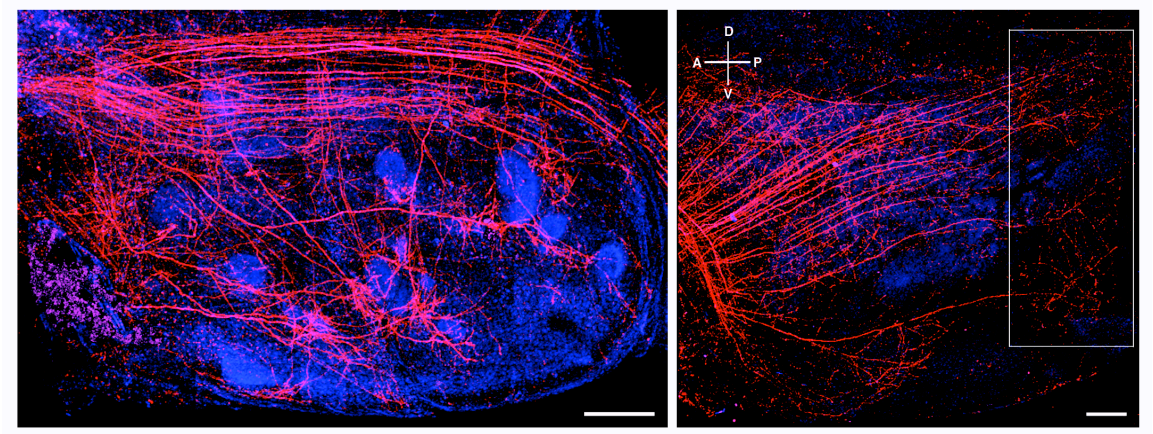

Supplementary Figure 3. Mitral/tufted cells elaborate distinct patterns of projection to the olfactory tubercle and lateral entorhinal cortex. The olfactory tubercle (left) receives two kinds of projections from the bulb. First, there are projections from individual cells that terminate in a claw-like tuft, often near the islands of Calleja (bright blue circles in tubercle). A second class of projections are less elaborate, with single axonal fibers that run across the tubercle from dorsal to ventral (scale bar = 400 μM). In both cases, projections cover the entire anterior-posterior extent of the tubercle. The lateral entorhinal cortex (boxed region in right image) receives different patterns of projections to its dorsal and ventral regions; projections that target the dorsal entorhinal appear disperse, regular and homogenous, while projections that target the ventral entorhinal cortex appear organized in a much less regular manner that is nest-like or web-like (scale bar = 800μM).

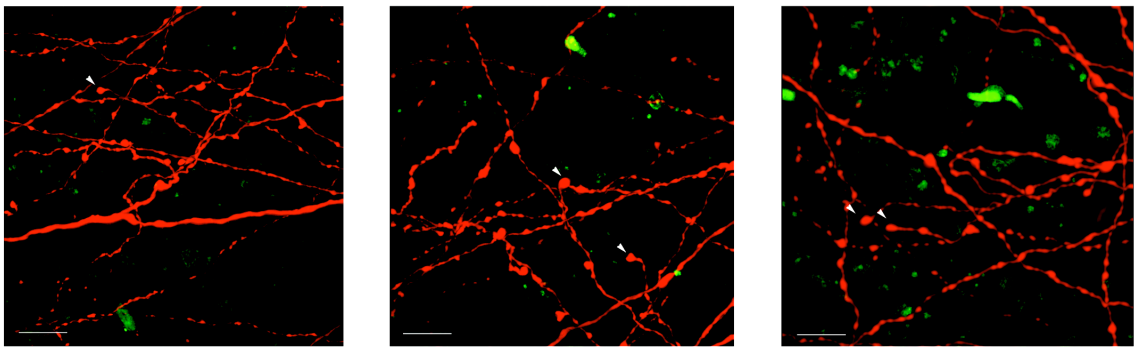

Supplementary Figure 4. High-resolution multiphoton imaging of mitral and tufted cell axons within the piriform cortex. Imaging at 120x (60x objective with 2x zoom) reveals structures likely to be axonal boutons, found both at axon termini (white arrows) and periodically along the length of axonal branches that have delaminated off of the lateral olfactory tract. Two images taken from different fields of view of the projections from the M72 glomerulus from the same animal (center and right) reveal strikingly similar anatomy, with boutons found wherever axons are found across the field of view; an image (left) of the projections from the MOR1-3 glomerulus in a different animal exhibits a similar distribution of boutons. Images of 20 separate fields from three separate animals each reveal similar distributions of boutons within the piriform (data not shown, see also Supplementary Figure 5), suggesting that synaptic distribution within the piriform may be similar to axonal branch distribution (scale bars = 10μM).

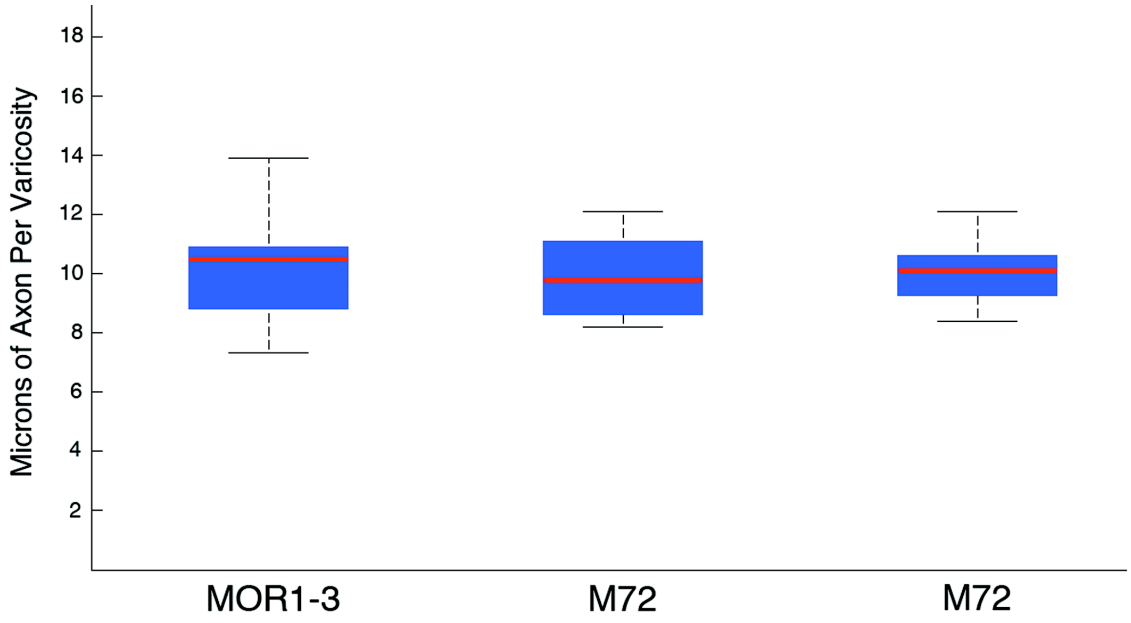

Supplementary Figure 5. The density of axonal varicosities in the piriform cortex is independent of glomerular identity. In the box plot, black bars represent the maximum and minimum values within the dataset, the blue box represents the 25th to 75th percentile, and the red bar represents the mean. Mean value of microns of axon per varicosity for the 1-3 glomerulus is 10.2 +/- .57 (n=10 fields of view, SEM), for one M72 glomerulus is 9.9 +/- .65 (n= 6 fields of view, SEM), and for a second M72 glomerulus is 10.1 +/- .36 (n=10 fields of view, SEM). By measuring the total area of the piriform, estimating the average length of axon per imaged field of view, and measuring the area of our field of view we can calculate the total number of potential axonal boutons per glomerulus within the piriform cortex. The total area of the piriform, as assessed using the contour surface function of Imaris on images of the whole piriform similar to Fig. 2, is 3.47 +/- .11 x10^{7} μM^2 (n=5 piriforms measured, SEM). The average number of microns per field of view (at 60x) is 3644 +/- 304 μM. Our field of view with a 60x objective is 3.72 x x10^{4} μM^2. These parameters result in a total number of boutons per glomerulus (assuming an

average of 10 μM axon per bouton) of 338,892 boutons per glomerulus per piriform cortex. It is critical to note that we count as a "bouton" any structure that appears to be 50% wider or more than the adjacent axonal width; if all such structures do not represent true boutons the actual number of synapses may be lower. However, both the number of boutons per unit length axon, and the resultant total number of boutons reported here likely represent an upper bound to the amount of connectivity between any given glomerulus and the piriform cortex.

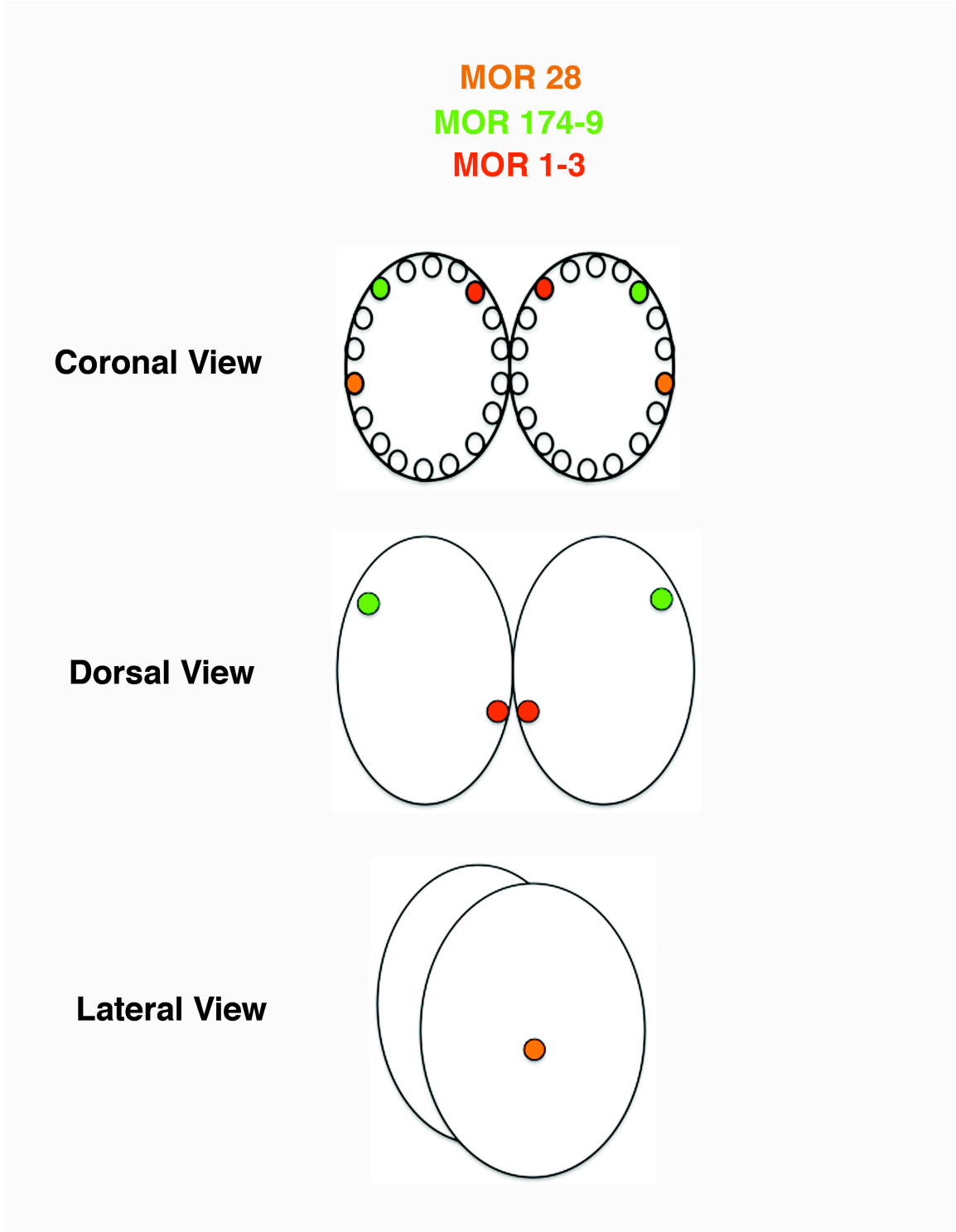

Supplementary Figure 6. Schematic of the olfactory bulb location of identified glomeruli targeted in experiments.

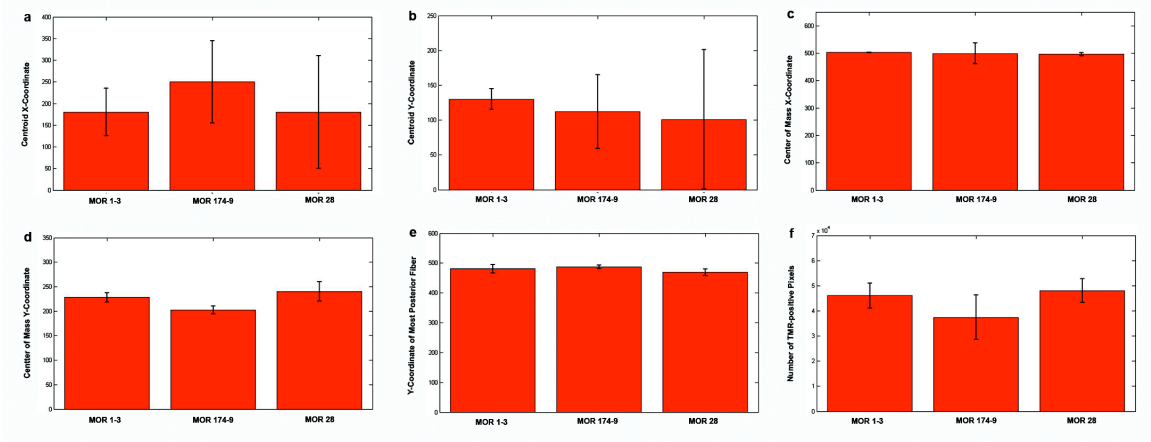

Supplementary Figure 7. Parameters extracted from aligned piriform cortex projection patterns are similar for all samples irrespective of glomerulus type. (a) Mean X-coordinate of centroid for MOR 1-3 (n= 4), MOR 174-9 (n =4), and MOR 28 (n=2) piriform projection patterns. **(b)** Y-coordinate of centroid. **(c)** X-coordinate of center of mass. **(d)** Y-coordinate of center of mass. **(e)** Y-coordinate of most posterior fiber. **(f)** Number of TMR-positive pixels. All errorbars = SEM.

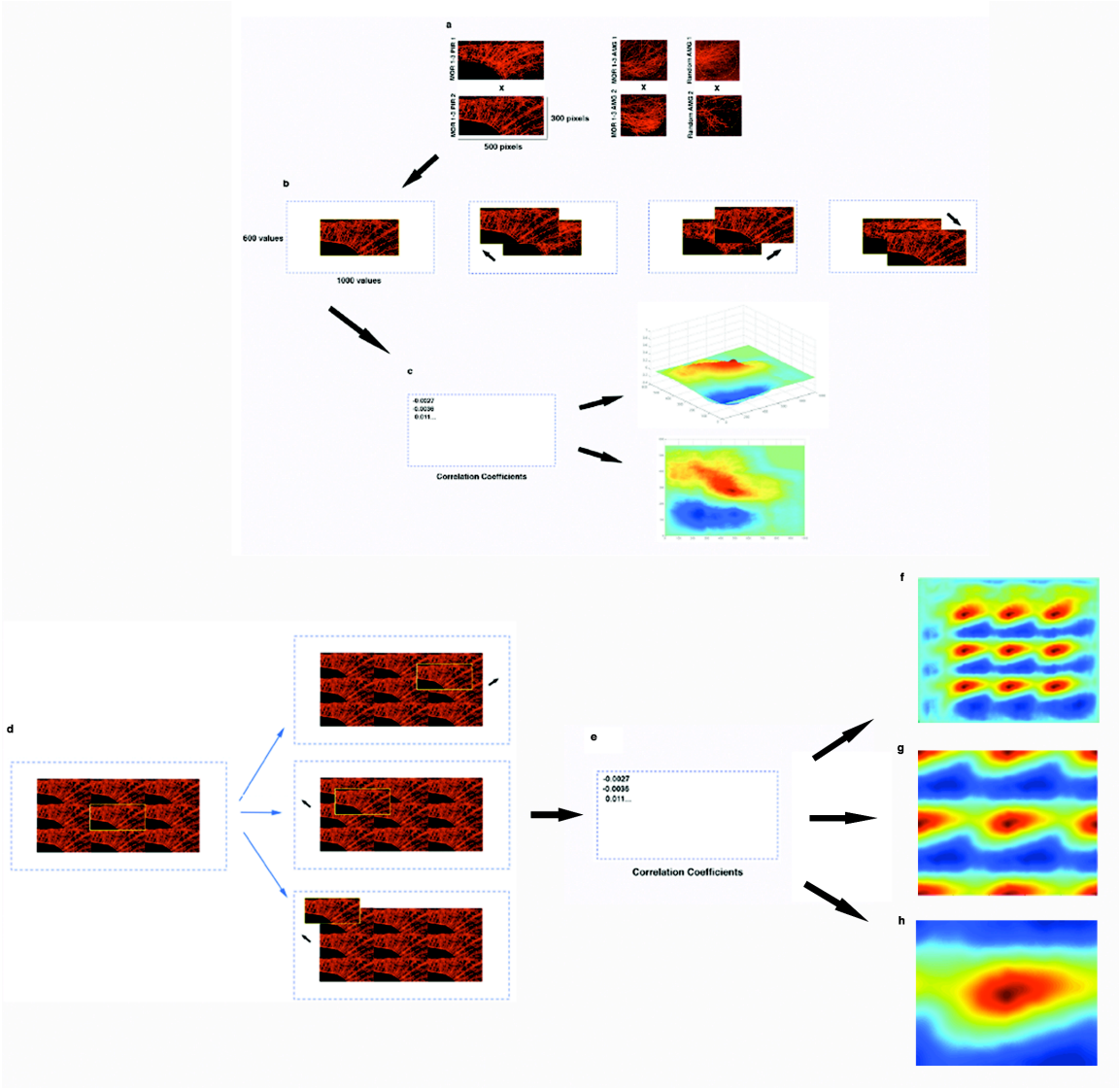

Supplementary Figure 8. Normalized cross-correlation analysis can be used to quantify the similarity of the spatial patterning in two images. (a) Examples of the images of piriform cortex and the posterolateral nucleus of the cortical amygdala used in normalized cross-correlation analysis. The source images are registered to a template image and filtered (see Methods) before being uploaded into Matlab, where they are represented as matrices of pixel values (e.g. piriform images would be represented as 500 x 300 matrices of pixel values if the images are 500 x 300 pixels in size). **(b)** The cross-correlation between the pixel values in each image is calculated when the images are

directly superimposed (left-most panel) and calculated again as one image is shifted relative to the other, repeatedly in all directions (e.g. one image is shifted to the top left, top right, bottom right, and so on, as illustrated). **(c)** The result of these calculations is a matrix of correlation coefficients. The size of the matrix of correlation coefficients is the sum of the lengths of the input source and template images in each axis minus one (e.g. a 500x300 source image correlated to a 500x300 template image would result in a 999x599 correlation matrix) because such a matrix can accommodate the entire range of possible spatial shifts of one image with regard to the other, while maintaining at least one pixel worth of overlap (e.g. if images were placed side by side lengthwise, the two images would be 1000 pixels long, and 600 pixels wide if the same was done for width). These correlation coefficients range from -1 to 1, with -1 reflecting perfect anticorrelation and 1 reflecting perfect correlation of pixel values. This matrix can be plotted as a correlogram (panels on right). Two ways of displaying this correlogram are illustrated; on top, a three-dimensional correlogram is used, where the correlation coefficient values are represented on the Z-axis, and the pixel values for width and length are represented on the X and Y axes, respectively. The data is plotted using a heatmap representation, where warm colors reflect locations of high pixel correlation, and cool colors represent areas of low correlation. Each location in the correlogram corresponds to the correlation coefficient calculated for a spatial shift of one image relative to the other (i.e. **(b)**). The bottom correlogram is simply the correlogram on top rotated 90 degrees towards the viewer. **(d)** Because normalized cross correlation analysis can be subject to edge artifacts where the two images have little overlap, we also implemented a data padding strategy to validate the data generated by traditional normalized cross correlation. By tiling the template, the

source image can be slid across the entire central template tile without the source image encountering a region of zero overlap. Because of the phasic nature of the tiled template image, the overall set of pixel values in the region of overlap is held constant, and therefore the mean image pixel value and the standard deviation of image pixel values used to calculate the Pearson coefficient **(e)** are also constant as this region of the tiled image slides across the template. While the source image will slide off the template at the edges (see **d**, bottom example), the source image never leaves the tiled template image as it samples the center tile. (**f**) Output correlograms from the tiled analysis appear to be a 3x3 array, with minor errors apparent at the edges; within this array an artifact-free tile appears in the center of the correlogram, and represents the correlation between the image and the template under conditions where the image never slides off the tiled template. **(g)** To directly compare the position of the maximum correlation coefficient between this method and the zero-padding method used in Figs. 3 and 4 we crop this correlogram such that it represents a similar spatial distribution of displacements. Note that the calculated values in the outer 50% of this correlogram represent displacements in which the source image overlaps more extensively with the outer tiles in the template than with the center tile, giving this correlogram a phasic appearance. The center tile, however, clearly lacks the edge artifacts apparent at the edges of **(f)**. **(h)** Cropping out the outer 50% of displacements from the image in **(g)** generates a correlogram in which the all of the included values represent an overlap of 50% or more of pixels between the image and the central tile. In this example of cross-correlation of two piriform cortices, this correlogram reveals a single peak in the center, consistent with this brain region containing similar patterns of projection.

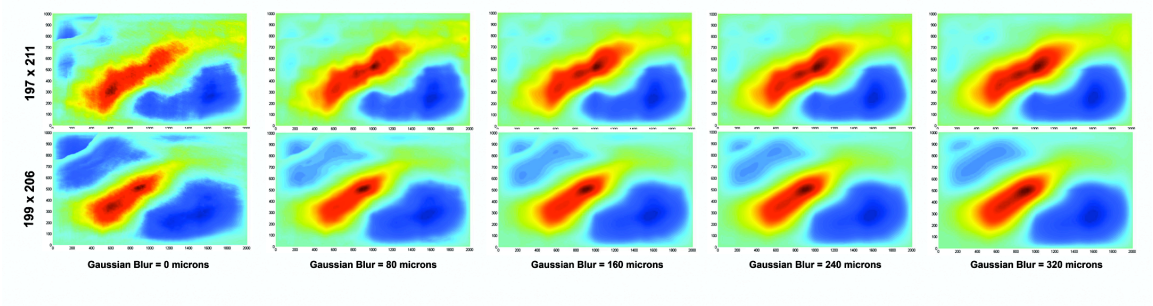

Supplementary Figure 9. The dispersed homogeneous pattern of projections to piriform cortex is seen across several spatial scales. (a) Correlograms from the normalized cross-correlation of two pairs of raw unblurred images of aligned piriform cortex projection patterns **(b)-(e)** Correlograms from normalized cross correlations of the same pairs of piriform projection pattern images after gaussian blurring (**(b)** σ = 80 μM; **(c)** σ = 160 μM; **(d)** σ = 240 μM; **(e)** σ = 320 μM).

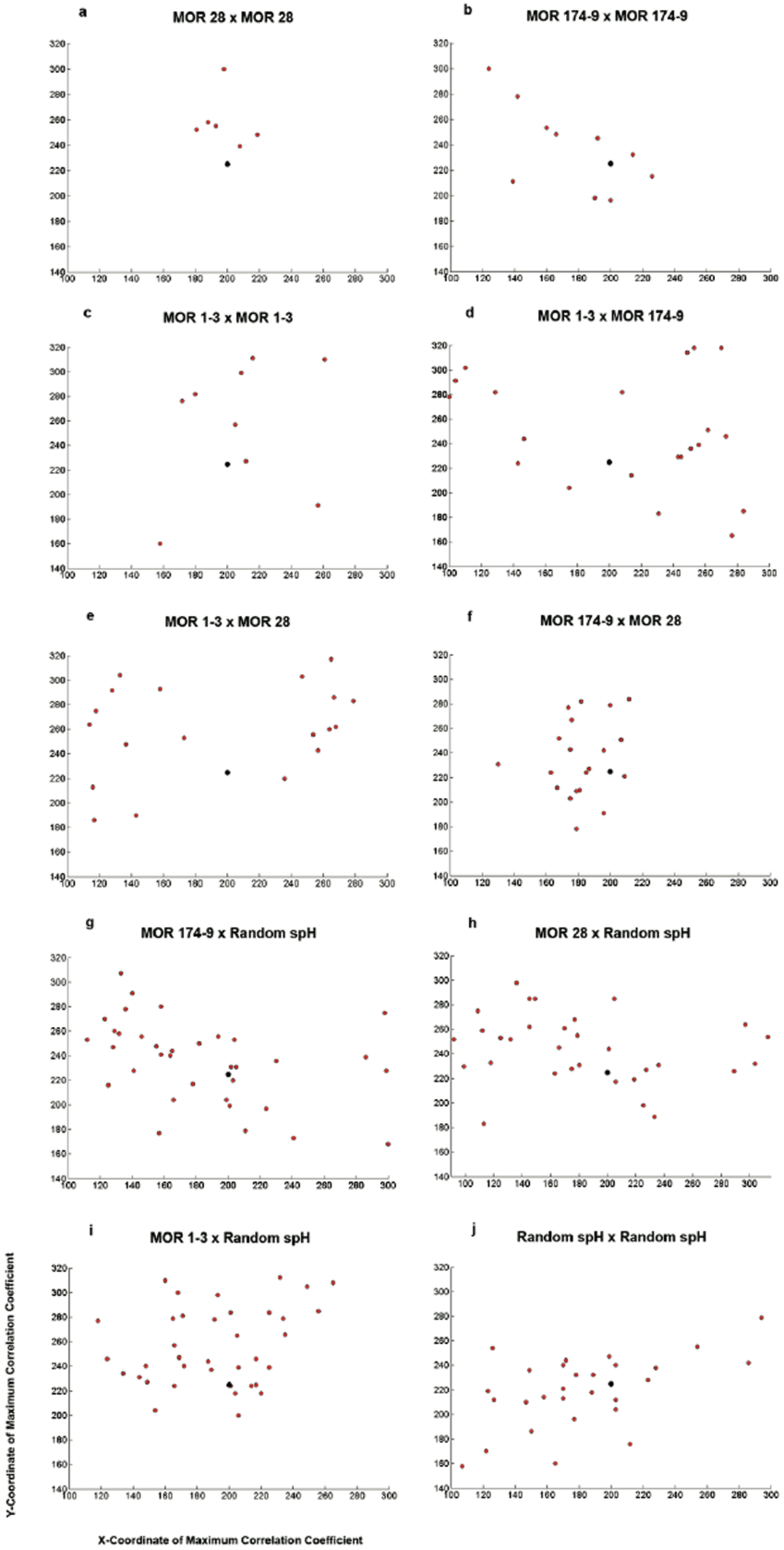
a
MOR 28 x MOR 28
b
MOR 174-9 x MOR 174-9
c
MOR 1-3 x MOR 1-3
d
MOR 1-3 x MOR 174-9
e
MOR 1-3 x MOR 28
f
MOR 174-9 x MOR 28
g
MOR 174-9 x Random spH
h
MOR 28 x Random spH
i
MOR 1-3 x Random spH
j
Random spH x Random spH
Y-Coordinate of Maximum Correlation Coefficient
X-Coordinate of Maximum Correlation Coefficient

Supplementary Figure 10. Correlograms generated by the normalized cross-correlation of posterolateral amygdala innervation patterns are more similar within than across glomerulus types when using two single images as the inputs for cross-correlation analysis. The location of the maximum correlation coefficient value in cross-correlograms is closer to the center of the correlogram (represented by black dot) and more homogeneous when cross-correlation is performed on two images from the same glomerulus **(a)-(c)** than when cross-correlation is performed using images from two different glomeruli **(d)-(j)**. **(f)** Note that MOR 28 x MOR 174-9 distances are similar to those seen for within-glomerulus comparisons; this is in accord with the large degree of overlap seen in the pattern of projections from these glomeruli in the posterolateral amygdala.

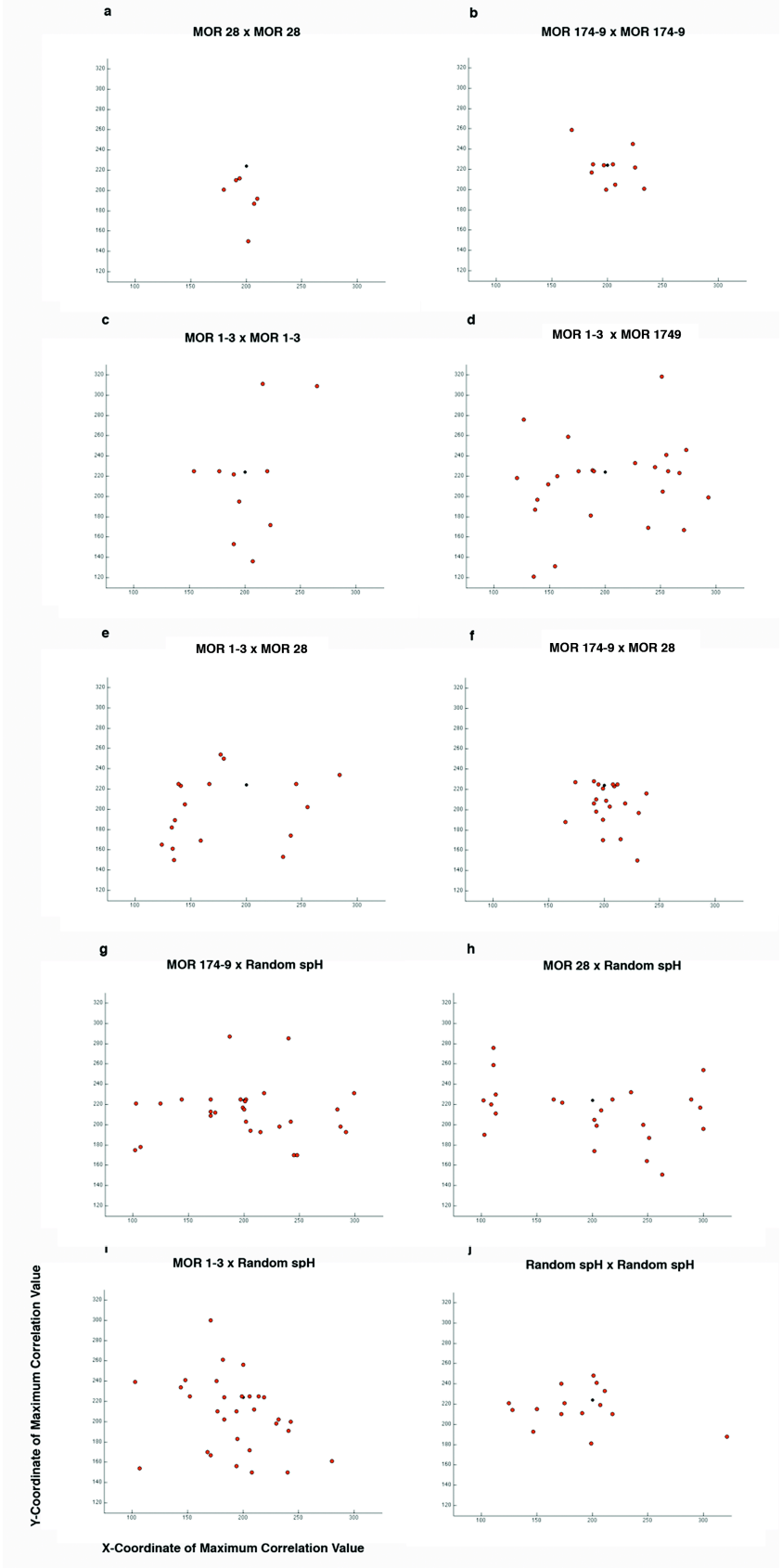
a
MOR 28 x MOR 28
b
MOR 174-9 x MOR 174-9
c
MOR 1-3 x MOR 1-3
d
MOR 1-3 x MOR 1749
e
MOR 1-3 x MOR 28
f
MOR 174-9 x MOR 28
g
MOR 174-9 x Random spH
h
MOR 28 x Random spH
i
MOR 1-3 x Random spH
j
Random spH x Random spH
Y-Coordinate of Maximum Correlation Value
X-Coordinate of Maximum Correlation Value

Supplementary Figure 11. Correlograms generated by the normalized cross-correlation of posterolateral amygdala innervation patterns are more similar within than across glomerulus types when using a single source image and a 3x3 tiled template image as the inputs for cross-correlation analysis. The location of the maximum correlation coefficient value in cross-correlograms is closer to the center of the correlogram (represented by black dot) and more homogeneous when cross-correlation is performed on two images from the same glomerulus **(a)-(c)** than when cross-correlation is performed using images from two different glomeruli **(d)-(j)**. Note the qualitative and quantitative similarity of the scatterplots generated using two different modes of normalized cross-correlation analysis (see Supplementary Methods, Supplementary Figure 11).

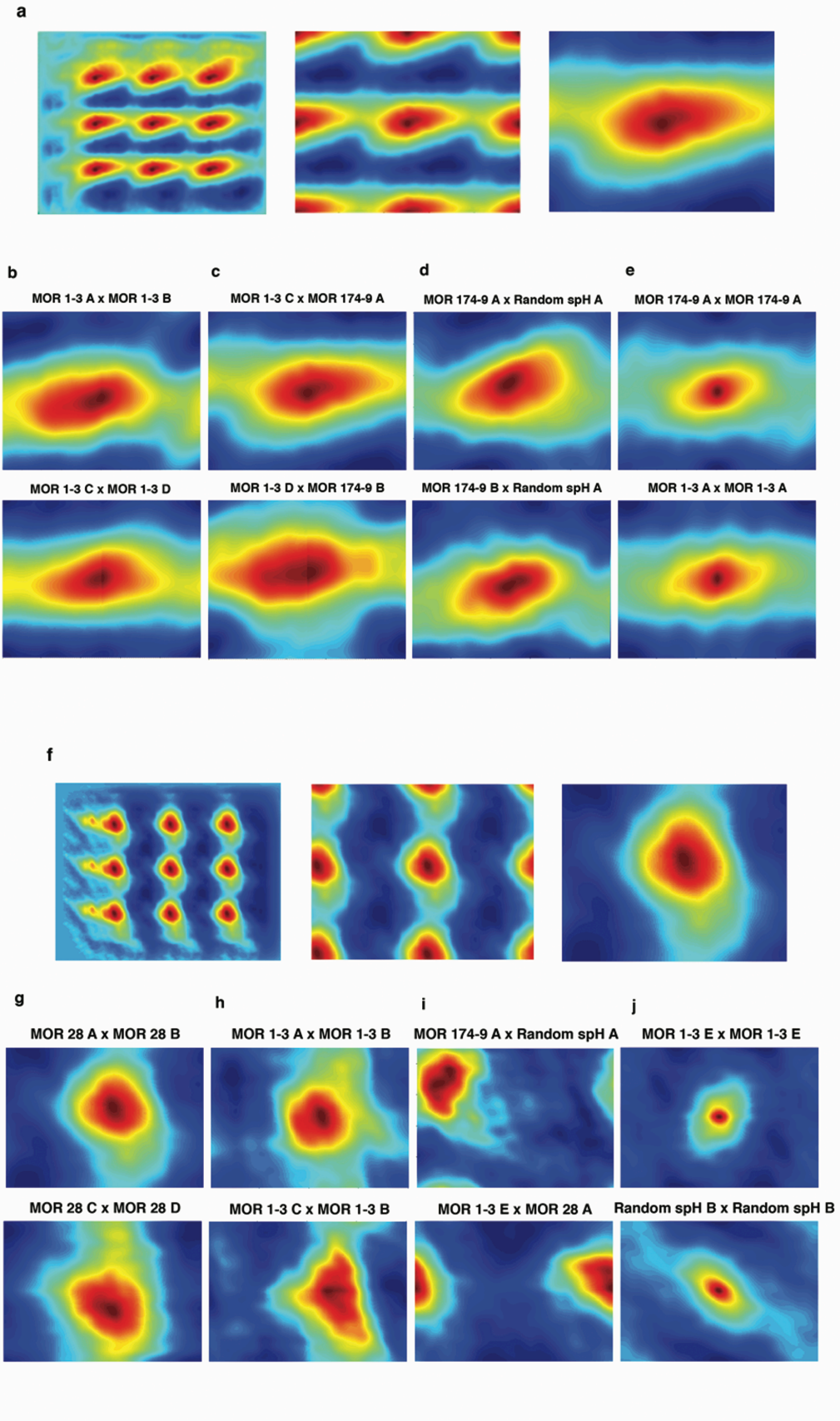
a
b
MOR 1-3 A x MOR 1-3 B
c
MOR 1-3 C x MOR 174-9 A
d
MOR 174-9 A x Random spH A
e
MOR 174-9 A x MOR 174-9 A
MOR 1-3 C x MOR 1-3 D
MOR 1-3 D x MOR 174-9 B
MOR 174-9 B x Random spH A
MOR 1-3 A x MOR 1-3 A
f
g
MOR 28 A x MOR 28 B
h
MOR 1-3 A x MOR 1-3 B
i
MOR 174-9 A x Random spH A
j
MOR 1-3 E x MOR 1-3 E
MOR 28 C x MOR 28 D
MOR 1-3 C x MOR 1-3 B
MOR 1-3 E x MOR 28 A
Random spH B x Random spH B

Supplementary Figure 12. Correlograms generated using a single source image and a 3x3 tiled template image as inputs for normalized cross-correlation analysis are similar to those generated using a single untiled template image. (a) Cross-correlation performed using a single projection pattern source image and a 3x3 tile of projection pattern images as the template image. This approach is used to address potential edge artifacts generated by non-overlapping pixels at the edges of the correlogram (See Supplementary Figure 8 for a comparison of this method and the zero-padding method). Output correlograms from the tiled analysis **(a, left)** appear to be a 3x3 array, with minor errors apparent at the edges, but an artifact-free tile in the center of the correlogram representing the correlation between the image and the template under conditions where the image never slides off the tiled template. **(a, center)** To directly compare the position of the maximum correlation coefficient between this method and the zero-padding method used in Figs. 3 and 4 we crop this correlogram such that it represents a similar distribution of displacements. Note that the calculated values in the outer 50% of this correlogram represent displacements in which the source image overlaps more extensively with the outer tiles than with the center tile, giving this correlogram a phasic appearance. The center tile, however, lacks the edge artifacts apparent at the edges of **(a, left)**. **(a, right)** Cropping out the outer 50% of displacements from the image in **(a, center)** generates a correlogram in which the all of the included values represent an overlap of 50% or more of pixels between the image and the central tile. In this example of cross-correlation of two piriform cortices, this correlogram reveals a single peak in the center, consistent with this brain region containing similar patterns of projection. **(b)** Spatial correlograms (top and bottom) plotted using the matrix of correlation coefficients

generated by normalized cross-correlation of two MOR 1-3 piriforms, and depicted using the 50% cropping method similar to **(a, right). (c)** Correlograms similar to **(b)** from cross-correlation of MOR 1-3 and MOR 174-9 piriforms. **(c)** Correlograms similar to **(d)** from cross-correlation of two piriforms of different glomerular types. **(e)** Autocorrelograms generated using methods similar to **(d)** in which a labeled piriform is compared to itself. **(f)** Images similar to those in **(a)** except comparing projection patterns within two amygdalae rather than two piriform cortices. **(g)** Spatial correlograms plotted using the matrix of correlation coefficients generated by normalized cross-correlation of MOR 28 projection patterns within the cortical amygdala. These data are depicted using the 50% cropping method, similar to **(b-e)**. **(h)** Correlograms similar to **(g)** from cross-correlation of MOR 1-3 projection patterns within the cortical amygdala. **(i)** Correlograms similar to **(g)** of PLCo projection patterns from different glomerulus types. Note that because the correlogram was cropped to only 50% of the potential overlap, where there are significant spatial shifts we observe that the peak appears to "wrap around" the correlogram, an effect that occurs because of the phasic nature of the tiled template. This result demonstrates that in many cases the correlation maximum for different glomeruli are actually offset from each other by more than 50% of the width of our raw images. **(j)** Autocorrelograms of the PLCo from two labeled glomeruli (top and bottom) correlated with themselves. Note that correlograms generated using a single source image and a 3x3 tiled template image are similar to those generated using two single images as inputs for both piriform cortex (**Figs. 3d-g**) and amygdala projection patterns (**Figs. 4h-k**).

Parameters Used in K-Means Clustering	Classification Success Rate
Center of mass X-coordinate, X-coordinate of first anterior fiber, y-coordinate of last posterior fiber	55%
Center of mass X-coordinate, number of TMR-positive pixels	55%
Center of mass X-coordinate, center of mass Y-coordinate, centroid X-coordinate, centroid Y-coordinate	55%
Number of TMR-positive pixels, X-coordinate of first anterior fiber, center of mass Y-coordinate	45%
Center of mass X-coordinate, center of mass Y-coordinate	55%
Y-coordinate of last fiber, X-coordinate of first fiber	55%
Y-coordinate of last fiber, X-coordinate of first fiber, number of TMR-positive pixels	45%
Centroid X-coordinate, centroid Y-coordinate	45%
Center of mass X-coordinate, center of mass Y-coordinate, X-coordinate of first fiber	63%
Center of mass Y-coordinate, Y-coordinate of centroid, Y-coordinate of last fiber	45%
X-coordinate of centroid, Y-coordinate of centroid, number of TMR-positive pixels	55%
Number of TMR-positive pixels	55%

Supplementary Table 1. K-means clustering is unable to correctly classify piriform cortex projection patterns according to glomerular identity regardless of what combination of parameters extracted from projection patterns is used.

	Variance of X Coordinate of Maximum Correlation Coefficient	Variance of Y Coordinate of Maximum Correlation Coefficient
MOR 28 x MOR 28	190.9	455.4
MOR 174-9 x MOR 174-9	1161.3	1163.8
MOR 1-3 x MOR 1-3	1234.9	2892.5
MOR 1-3 x MOR 28	4237.2	2142.2
MOR 1-3 x MOR 174-9	4603.7	2403.8
MOR 28 x MOR 174-9	330.9	976.7
Mean Within Glomerulus Type	862.3 +/- 412	1503.9 +/- 886.4
Mean Across Glomerulus Type	3057.3 +/- 1674.6	1840.9 +/- 537

Supplementary Table 2. The variance of the distributions of the X and Y location of the maximum correlation coefficient in correlograms (plotted in Supplementary Figure 11) is greater when comparing across glomerulus type than when comparing within glomerulus type (X/Y location calculated from correlograms generated using two single images for normalized cross-correlation analysis).

	Variance of X Coordinate of Maximum Correlation Coefficient	Variance of Y Coordinate of Maximum Correlation Coefficient
MOR 28 x MOR 28	125.5	518.8
MOR 174-9 x MOR 174-9	402.9	350.9
MOR 1-3 x MOR 1-3	910.2	3409.0
MOR 1-3 x MOR 28	2717.4	1158.2
MOR 1-3 x MOR 174-9	2986.4	1758.5
MOR 28 x MOR 174-9	324.6	473.0
Mean Within Glomerulus Type	479.5 +/- 281.4	1462.2 +/- 1215.6
Mean Across Glomerulus Type	2009.5 +/- 1036.2	1130.0 +/- 454.8

Supplementary Table 3. The variance of the distributions of the X and Y location of the maximum correlation coefficient in correlograms (plotted in Supplementary Figure 12) is greater when comparing across glomerulus type than when comparing within glomerulus type (X/Y location calculated from correlograms generated using a single image and a 3x3 tiled image for normalized cross-correlation analysis).

Supplementary Movie 1. Animated Z-stack that descends from the surface of the olfactory bulb past the mitral cell layer of the bulb after electroporation of a single glomerulus. Red = TMR dextran, green = synapto-pHluorin label.